Local atomic structure deviation from average structure of Na_{0.5}Bi_{0.5}TiO_{3}: Combined x-ray and neutron total scattering study

Elena Aksel, Jennifer S. Forrester, Juan C. Nino, Katharine Page, Daniel P. Shoemaker, and Jacob L. Jones

Phys. Rev. B **87**, 104113 — Published 27 March 2013

DOI: 10.1103/PhysRevB.87.104113

Local atomic structure deviation from average structure of $Na_{0.5}Bi_{0.5}TiO_3$: a combined X-ray and neutron total scattering study

Elena Aksel[1], Jennifer S. Forrester[1], Juan C. Nino[1], Katharine Page[2], Daniel P. Shoemaker[3] and Jacob L. Jones[1*]

[1]*Department of Materials Science and Engineering, University of Florida, Gainesville, FL 32611, USA*
[2]*Lujan Neutron Scattering Center, Los Alamos National Laboratory, Los Alamos, NM 87545,USA*
[3]*Materials Science Division, Argonne National Laboratory, Argonne, IL 60439, USA*

Abstract

The crystal structure of sodium bismuth titanate and related compounds is of great interest, as these may form part of a new generation of ferroelectric materials used in a multitude of piezoelectric applications. This work examines the short and long range structure of sodium bismuth titanate in different states of synthesis using X-ray and neutron pair distribution function studies. The average structure of NBT was modeled using the monoclinic *Cc* space group through a combined structural refinement of X-ray and neutron diffraction data via the Rietveld method. A small box approach was used to model the local structure based on the average structure of the material, as determined from the Rietveld structural refinement, and rule out the presence of local A-site ordering in NBT. A 'box-car fitting' method used to analyze the neutron PDF showed that bond environments change when averaged over different length scales and the calculated bond valence of Bi^{3+}, in particular, is different locally from its average value. A model calculated using the Reverse Monte Carlo method allowed the positions of Na^+ and Bi^{3+} to move independently, allowing the determination of their distinctive bonding environments with O^{2-}. This method revealed that Na^+ and Bi^{3+} have slightly different atomic positions, an effect that may be the origin of the large atomic displacement parameters calculated for the A-site from the

* Corresponding Author: email jjones@mse.ufl.edu, telephone 352-846-3788

average structure model. The local structure described here is discussed in comparison with published long-range structure models.

I. Introduction

Sodium bismuth titanate (NBT) is one of the leading candidates currently being investigated as a lead (Pb)-free alternative to the commonly used lead zirconate titanate (PZT) piezoelectric composition.[1] Although this material was first reported in the 1960s,[2] there is still much debate over its structure. NBT was originally considered to have a rhombohedral room temperature structure in the *R*3*c* space group.[3] However, more recent studies using high resolution diffraction techniques report that the room temperature structure of this material is more closely described using the monoclinic *Cc* space group.[4,5] The structure of NBT appears to be even more complex with reports of a unique short range structure in this material.[6-8] A study using selected area electron diffraction in transmission electron microscopy (TEM) found the presence of nano-scale platelets of tetragonal (*P*4*bm*) structure within the NBT matrix (*R*3*c* or *Cc*) at room temperature.[6] This finding was supported by studies of NBT single crystals through diffraction contrast images in TEM.[7] In a more recent report, the nanoscale twin domains are interpreted as local regions of $a^-a^-c^+$ tilting with a coherence length of only a few unit cells, with assemblages of these structures yielding the long-range *Cc* space group and $a^-a^-c^-$ octahedral tilting.[8] Also, first-principles calculations based on density functional theory (DFT) were utilized to examine the extent of A-site ordering and concluded that short range chemical ordering is favorable.[9] However, the observation of A-site ordering has been refuted using high angle annular dark field imaging in a scanning TEM.[8]

Total scattering methods are now well-recognized tools capable of extracting reliable and meaningful information on the short range order of complex materials.[10-12] Pair distribution function (PDF) studies have been utilized to probe local structural distortions[13] and ordering[14] in a variety of perovskites, including different ferroelectric materials.[15-19] Recently, Jeong *et al.*

compared the short range structure of NBT to that of its solid solution with $Bi_{0.5}K_{0.5}TiO_3$ through neutron total scattering studies with Reverse Monte Carlo (RMC) modeling.[20] They reported that the bonding environment of Bi with O is different from that of Na with O when examined on a <4 Å length scale, due to a large displacement of Bi from its average position.[20] Keeble *et al*. further examined the difference in the local environments of Na and Bi in NBT by comparing stereographic projections of the directions of displacement of the two A-site ions obtained from RMC models of neutron PDF data.[21] They report that while Na mainly displaces within a monoclinic plane, Bi has two distinct distortions, one in the monoclinic plane and another approaching an orthorhombic direction.[21] These PDF results support an earlier study from Shuvaeva *et al*. in which the local environment of Bi in NBT was analyzed using X-ray absorption fine structure (XAFS).[22] According to Shuvaeva, the shortest Bi-O bond determined through XAFS is 0.3 Å shorter than what is expected from conventional diffraction studies.[22] They therefore suggested that Bi has a local environment which is far more distorted than what is expected from its average structure.[22] Total scattering methods such as PDF are able to provide additional information about such displacements, such as the atomic species being displaced and the crystallographic direction of displacement.

A complete structural description of NBT must account for mixed A-site occupancy of Bi^{3+} and Na^{+}. Because the X-ray scattering factors of Bi^{3+} and Na^{+} are significantly different (i.e., 62.425 Bi^{3+} fm and 6.881 Na^{+} fm)[23], X-ray scattering can best be used to distinguish these ions. However, X-rays are not sensitive to O^{2-} (i.e. a scattering factor of 4.089 fm for O^{2-})[23], and neutrons more reliably characterize oxygen positions and occupancies in materials because O^{2-} has a neutron scattering factor comparable to the other ions (i.e. 5.80 fm for O^{2-}, 3.63 fm for Na^{+}, and 8.53 fm for Bi^{3+}, and -3.44 fm for Ti^{4+})[24]. The unique weighting of atomic contributions in

X-ray and neutron scattering data make a combined analysis approach advantageous for examining both A-site ordering and the oxygen positions around this site. It is also of interest to compare the local structure of this material during different synthesis steps (e.g., after phase formation or calcination of the particles, and after sintering and densification of polycrystalline materials) to examine the possible influences of strain, grain growth, and other factors during sintering. The PDF approach provides the sensitivities necessary in the present work to probe the local structure of NBT at different synthesis steps. This local structure is also then compared to the structure determined from a crystallographic refinement using combined neutron and X-ray diffraction data. The results provide insight into the evolution of the local and long-range or average structure during the synthesis of an important ferroelectric composition.

II. Experimental Methods

Materials were prepared using solid state synthesis techniques described previously in Davies *et al*.[25] Reactant powders, Bi_2O_3 (99.975% purity, Alfa Aesar, Ward Hill, MA), TiO_2 (98% purity, Fisher Chemical, Pittsburgh, PA), and Na_2CO_3 (99.5% purity, Alfa Aesar) were first calcined at 800ºC for 2 h and some powder was retained for structural characterization after this synthesis step (hereafter referred to as "calcined"). Samples were then also sintered and densified into pellets at 1100ºC for 1 h. The sintered pellets were crushed into powder and annealed at 400ºC for 3 h in a closed alumina crucible in order to thermally anneal any possible residual stresses induced by the grinding process (hereafter referred to as "sintered"). X-ray diffraction patterns of calcined and sintered powders of NBT were measured at beamline 11-BM at the Advanced Photon Source (APS) at Argonne National Laboratory using the sample preparation, instrumental parameters and wavelengths (0.458739 Å for calcined and 0.413629 Å

for sintered) described previously in Aksel *et al*.[5] Two grams of each powder sample were loaded into vanadium cans and neutron scattering data were measured for approximately 8 h at room temperature on the neutron powder diffractometer NPDF[26] at the Lujan Center at Los Alamos National Laboratory. Extraction steps were followed in order to obtain the experimental pair distribution function from scattering data utilizing the program PDFgetN[27] and a Q_{max}= 35 $Å^{-1}$.

X-ray PDF measurements were completed at room temperature at the 11-ID-B beam line at the APS using a General Electric amorphous Si two-dimensional (2D) detector. The sample to detector distance was fixed at 117.13 mm, and synchrotron X-rays with the wavelength of 0.2127 Å were utilized with a 0.2 mm x 0.2 mm beam size. Each measurement was carried out in multiple exposures then 2D datasets were integrated using the program FIT2D.[28] The program PDFGETX2[29] was used with standard corrections to extract the experimental PDF using a Q_{max}=22 $Å^{-1}$.

Modeling of the average structure of NBT was done using the Rietveld analysis program GSAS.[30, 31] A refinement of the structure was completed using the *Cc* space group by the method described in Aksel *et al*.[5] In the present work, however, the refinement combined both the X-ray and neutron diffraction patterns for each sample. Least-squares refinements to the experimental PDF data were carried out with the aid of PDFgui software.[32] Calibration of the NPDF and 11-ID-B instrument using standard samples provided parameters describing the PDF dampening envelope due to instrument resolution and the PDF peak broadening due to intensity noise.[33] These parameters were fixed during analysis. RMC simulations were performed using RMCprofile[34] with 5 x 10 x 10 supercells starting from the Rietveld-refined *Cc* structure, with 10,000 total atoms in each supercell. These simulations were fit to D(r) in the convention of

Keen[35] and run for 16 h on single 2GHz cores (about 2.4×10^7 moves). Simulations were constrained by periodic boundary conditions and hard-sphere nearest neighbor cutoffs, but not by lattice symmetry. No bunching occurred at the hard-sphere distances. RMC fits were performed for neutron data only, since it offered better resolution (higher usable limit of momentum transfer Q) and similar cross-sections for each atom. A weak bond valence constraint (parameters obtained from Brese and O'Keefe[36]) was applied to prevent coordinations that produce a Na valence greater than 1+. Bi occupies a more anisotropic environment than Na regardless of constraints on bond valence.

III. Results and Discussion

A. Rietveld Analysis

Diffraction patterns measured for both calcined and sintered NBT are shown in Figure 1. As previously described in Aksel *et al*.,[5] calcined powders have a higher sample contribution to peak broadening. Therefore, the insets of the X-ray measurements in Figure 1 show a clearer peak splitting in the sintered powders. Due to this lack of peak splitting, the calcined pattern can be fit to a lower weighted residual, R_w, value. The long-range average structure of each of the calcined and sintered materials was determined using a combined Rietveld refinement of the X-ray and neutron diffraction patterns. A closer examination of the diffraction patterns on a logarithmic scale (not pictured) shows a large modulation in the background due to diffuse scattering in the material, indicating that NBT may have a local structure which differs from the average structure.

The observed Bragg intensities were used to create Fourier maps of the NBT *Cc* cell using both neutron and X-ray data (Fig. 2). These agree well with the previously-published *Cc*

space group that describes the average crystallographic structure on a long-range length scale.[5] The Fourier maps display scattering density in the unit cell, and symmetry of these maps is determined by the space group. All atoms in the NBT *Cc* cell lie on 4*a* Wyckoff positions with site symmetry 1 (no symmetry constraints), so any off-centering or static displacements should be evident in large, anisotropic, or irregular isosurfaces of scattering density on each site. Instead, only spherical scattering density is seen at each site. Large Bi^{3+} displacements would be especially evident in the X-ray Fourier map due to its large cross section. The small spherical isosurfaces seen here suggest that simply adding A-site displacements alone should not help to describe any disorder in the *Cc* model (which already contains a very asymmetric Bi^{3+} coordination in the average structure).

B. Small Box PDF Modeling

The pair distribution functions measured for calcined and sintered NBT using both X-ray and neutron total scattering are shown in Figure 3 on a 1-20 Å range. The X-ray and neutron results have very different peak intensities due to the distinctly weighted scattering factors of the two methods for different atoms. A brief comparison of the calcined and sintered results does not show any obvious differences between the two measurements. The experimental X-ray and neutron PDFs were initially fit using PDFgui with the average *Cc* structure model resulting from Rietveld analysis. The lattice parameters, atomic positions, and atomic displacement parameters were refined using the neutron PDF data within the setting of the *Cc* space group (Fig. 3(c) and 3(d)) in PDFgui. Similar parameters were used for the X-ray PDF data refinement (Fig. 3(a) and 3(b)), except the atomic positions of O^{2-} ions were fixed to those resulting from the neutron

refinement and isotropic O^{2-} atomic displacement parameter were constrained to be equivalent among the three unique O^{2-} sites.

The results of the initial fitting, displayed in Figure 3, lead to several observations. First, in all cases the structure model describes the higher-*r* region of the PDF more closely than the lower-*r* region of the PDF, suggesting a departure of the local atomic structure from the long-range average structure. This is consistent with the observed presence of diffuse scattering in the diffraction patterns of the material. Second, the X-ray PDF data (top panels) are more poorly described using the average structure model than the neutron PDF data (bottom panels). This suggests Bi^{3+} ions (much more heavily weighted in the X-ray data than in the neutron data) may have a prominent role in the local atomic disorder. Finally, a comparison of the R_w values and the difference curves for the model fits of both X-ray and neutron $G(r)$ functions indicates that the sintered powders are better described by the average structure model than the calcined powders. This suggests there is a larger departure from the long-range structure in the calcined material, which exists prior to the heat treatment step at 1100ºC.

Inspection of the atomic positions and displacement parameters from the Rietveld (long-range crystal structure) and PDF refinement (local atomic level structure), presented in Tables I and II, allows a comparison between the atomic position and displacement parameters calculated in the PDF fit to those calculated using the Rietveld method. The Na/Bi atomic displacement parameter in the PDF refinement is much lower than that of the Rietveld refinement. This suggests that the refinement of oxygen positions results in a more realistic local environment for the A-site in the PDF model.

Several different local structure models were employed to understand the departure of the local atomic structure from the long range average structure, as well as the differences between

calcined and sintered conditions. First, the influence of *A*-site ordering was explored because there is evidence of short-range ordering of the A-site reported from DFT calculations.[9] The results of one such model using the sintered structure are given in Figure 4. In order to create a model of an ordered structure, the experimental average structure of sintered NBT was first refined in PDFgui with random A-site ordering using the 1-10 Å range in the PDF (corresponding to fraction layered phase = 0 in Fig. 4(a)). The A-site atoms of the refined structure were then changed into a layered arrangement with layers perpendicular to the monoclinic c-axis (as shown in Fig. 4(a)). The same region of the PDF was then modeled by varying the phase fractions of the ordered and disordered phases while maintaining all other parameters constant.

In Figure 4(a), the trend in R_w of the fit with varying phase fractions of the ordered and disordered phases is shown. For both calcined and sintered samples, the agreement factor between observed and calculated X-ray data is increasingly disparate as the fraction of layered phase is increased during modeling. There is little change observed between the agreement factors for the neutron data. Figures 4(b) and 4(c) demonstrate that neutron PDF is not as sensitive to this configuration of atomic ordering as the X-ray PDF. Further inspection of the 6-7 Å region of the calculated X-ray PDFs shows that the random model allows for a larger split in the peak with a larger intensity at the higher *r* side. A comparison of this feature with the measured PDF shown in Figure 3 indicates that this feature of the random model is consistent with the measurement. Although a number of other superstructures were tried with chemical short range ordering of the A-site cations, none were found to better describe the data than the model with fractionally occupied (shared) sites. Since A-site ordering was not beneficial in improving the PDF fit of NBT, it is not considered to be the source of the deviation of the local

structure in these samples. This result is also consistent with the prior work of Levin and Reaney.[8]

Since A-site ordering is not the source of the local structure deviation, another approach, the so-called '*r*-range refinement' or 'box-car fitting' was utilized to examine A-O and Ti-O bonding behavior with the neutron PDF data. Box-car fitting is a method that is used to extract quantitative information about the *length scale* of local atomic order from the PDF analysis of complex materials.[37] In order to extract information about the local cation bonding environments in NBT, the neutron PDF was first modeled using only the 1-11 Å range. The neutron PDF is then fit by refining the structural model over separate and successive 10 Å intervals in real space. The PDF of the first 1-6 Å was also refined separately for comparison. In this range, the step size is small compared to the unit cell dimensions (>5 Å). Thus, lattice parameters in the 1-6 Å range were constrained to the values obtained from the refinement in the 1-11 Å range and the atomic positions and displacement parameters were refined. In all of the other interval ranges, the lattice parameters, atomic positions, and atomic displacement parameters were refined in order to evaluate these variables as a function of length-scale in the material.

Figure 5 presents box plots of the bond lengths extracted from the 'box-car fitting' of the neutron PDF data over increasing intervals in real space. The averages (shown in the insets) and standard deviations (indicated by the edges of the boxes) are calculated from the six unique Ti-O bond lengths and the 12 unique (Bi/Na)-O bond lengths. Since the bond lengths with oxygen are of interest and the Na/Bi position is constrained, the neutron PDF was used for this analysis rather than the XRD PDF due to the previously mentioned higher sensitivity to the oxygen positions. The error bars shown for the average bond lengths in the insets of the figure are propagated from the error calculated for each bond length in the refinement. The spread in the

bond distances is also highlighted by the whiskers of the boxes, which represent the minimum and maximum value found with each *r* interval.

It is clear from the insets of Figure 5 that the average bond lengths found for (Bi/Na)-O are longer in the first 10 Å range than at higher *r* ranges. A similar, but less pronounced trend is also observed in the Ti-O bond lengths. In addition, at lower *r* values, the spread in the (Bi/Na)-O bond lengths is greater compared to the higher *r* range. A comparison between calcined and sintered powders indicates that while the average (Bi/Na)-O bond lengths in the first 10 Å are slightly larger in calcined samples, the spread in the bond lengths at high *r* is less for the calcined powders than sintered powders. The results for higher *r* in both the calcined and sintered powders are consistent with the average structure calculated using the Rietveld method. Also, it should be noted that the spread in the (Bi/Na)-O bond lengths is much greater than that in the Ti-O bond lengths, indicating significant Bi disorder.

The bond lengths calculated from the average structure and the 'box-car fitting' of the neutron PDF were used to determine the bond valence sum (BVS)[38] of Bi^{3+}, Na^{+}, and Ti^{4+} from different length scale models. The results of these calculations as a function of *r* are given in Figure 6. In the average structure, Bi^{3+} has a BVS of 2.26 in calcined and 2.33 in sintered NBT, which is significantly lower than the ideal value of 3. On the other hand, Ti^{4+} has a BVS of 4.05 in calcined and 4.01 in sintered NBT, rather than the ideal value of 4. The change in the refined bond length of (Bi/Na)-O on the local scale seen in Figure 5 may therefore be due to A-site or O^{2-} atomic motion, allowing for a higher BVS for Bi^{3+}.

It is important to note that, since this is a small box approach, the Bi^{3+} and Na^{+} positions are constrained to be identical in the model. This is a significant limitation because accommodation of the Bi^{3+} lone pair often results in distorted Bi-O coordination, and thus local

dipoles, but no such disorder is expected for Na^+. While this type of cation-specific structural information cannot be easily determined using a small box approach, it can be examined using RMC analysis, as discussed in the next section.

C. Reverse Monte Carlo Modeling

In order to observe the distinct atomic arrangements that give rise to the low-*r* disorder observed in this system and accommodate the different bonding environments of Bi and Na, RMC refinement of the neutron PDF was employed. Fits to data from calcined and sintered samples are shown in Figure 7. These fits reproduce the experimental data more closely than the least-squares refinements in Figure 3 because the large-box RMC model is not constrained by *Cc* symmetry, enabling many more degrees of freedom. No significant differences are observed between calcined and sintered samples. In both the calcined and sintered cases, bond valence sums indicate average positive valences of 1.39, 3.09, and 3.99 for Na, Bi, and Ti, respectively. Since the Na valence is far from its expected value, new simulations were run with BVS constraints applied such that each cation is fixed to its nominal valence over the entire course of the RMC simulation. The fits to data shown in Figure 7 were performed with BVS constraints applied, and no difference in the quality of fit is seen versus BVS-unconstrained simulations. Therefore, results in all the figures are given for simulations where the valences of all cations are constrained to be within +/-0.05 of the nominal values of Na^+, Bi^{3+}, and Ti^{4+}.

Folding the large RMC model into a single unit cell produced "point clouds" of approximately a thousand atoms at each crystallographic site. These are plotted as a function of real space for a sintered sample in Figure 8. Only Na atoms are shown on the A-sites in Figure 8(a), and only Bi are shown in Figure 8(b). The point clouds of Na and Bi both appear spherical

with no obvious difference in their cation distributions. This observation suggests that the differences in Na/Bi coordination are not strong. That interpretation is corroborated by the Fourier map of Bragg scattering in Figure 2, which shows a spherical neutron and X-ray cross-section on the A-sites, implying that Bi^{3+} tends to remain in its average position in the *Cc* structure. In the previous work by Jeong *et al*., Bi^{3+} was shown to have a large degree of directional off-centering, because that displacement is described relative to the high-symmetry *R*3*c* structure. Our results in the present work are built upon the average *Cc* starting model, which was determined from Rietveld refinements to the Bragg diffraction pattern.[20] The "large displacement" seen by Jeong *et al*. with respect to a the higher-symmetry *R*3*c* cell[20] are contained within the average structure of the *Cc* model, which contains a highly distorted (and coherent, long-range ordered) Bi environment in the average structure. This difference between the two models provides further support for the classification of NBT in the monoclinic *Cc* space group. Consequently, the asymmetric Bi^{3+} environment is obtained without incoherent Bi^{3+} displacements which had been reported for other Bi^{3+} containing materials such as the pyrochlore $Bi_2Ti_2O_7$.[39]

Since the RMC model contains thousands of distinct Na and Bi cations, each with a unique coordination, the *partial* pair distribution functions $n(r)$ that show only Na-O or Bi-O distances found in the simulated model can be selectively plotted. These distributions are shown in Figure 9. Each distribution is divided into three curves, showing the bond distances of Na and Bi to the three distinct O anions in the 4*a* Wyckoff positions in the *Cc* cell. Between the panels of Figure 9, vertical ticks show the *A*-O bonds present in the *Cc* cell (they apply to both Na^+ and Bi^{3+} in the average structure) as determined from Rietveld refinement of the combined diffraction data. The partial pair distributions are broader than the *A*-O distances from the

average structure due to thermal motion and instrumental broadening. Na-O bonds are nearly symmetric about their average distance, while, Bi-O bonds are more asymmetric than the *Cc* model suggests. A fairly large portion of the Bi-O distribution is shifted towards bond lengths which are shorter than suggested by the average structure. This result is consistent with the previous findings of Shuvaeva *et al*. using XAFS.[22]

In order to determine the origin of the two distinct *A*-O bonding environments, the Na^{+} and Bi^{3+} point clouds from Figure 8 are further investigated. Figure 10 describes the distribution of the Na^{+} and Bi^{3+} ions relative to the average A-site position, where the x and y directions are along the *a* and *b* unit cell axes, and z is orthogonal to them. Along y and z there is no discernible difference in the Na^{+} and Bi^{3+} distributions. However, in the x-direction there is a noticeable shift in the center of the Na^{+} from the average position. This shift can be related to the *A*-O bond length distribution (Fig. 9) as moving towards the longer *A*-O bonds. The center of the Bi^{3+} distribution is also shifted slightly from the average position, but in the opposite direction from the Na^{+} shift. The shift in the Bi^{3+} center can be described as moving towards the shorter *A*-O bonds. The movement of Na^{+} towards the far O^{2-} position implies that it is approaching the center of its surrounding O^{2-} environment, while Bi^{3+} remains off-center. This result, in combination with the small box BVS calculation, means that Na and Bi each shift slightly from their average crystallographic position to form unique bonding environments with the surrounding oxygen atoms. This enables both Na^{+} and Bi^{3+} to satisfy the sum charge of their bonds with O^{2-}. The long-range *Cc* structure appears to be an average of the two disparate cation environments of Na^{+} and Bi^{3+}.

A closer examination of the partial PDF of Bi^{3+} with O^{2-} (Figure 9(b)) reveals another distinction in the distribution of bond lengths. The Bi-O1 and Bi-O2 bond lengths have bimodal

distributions with approximately equal intensity of each mode. The Bi-O3 bond lengths are also bimodal, but with a more disparate intensity of the two modes. The bond distances calculated from the average structure (shown in Figure 9 as the tick marks between parts a and b) exhibit similar bond distance splitting. The average Bi-O1 and Bi-O2 bond lengths have a short and long bond, but the Bi-O3 bond lengths center around one value. To compare the relation of the three oxygen positions around the A-site, the different configurations are shown in a pseudo-cubic unit cell in Figure 11. It can be seen that the O1 and O2 ions lie outside of the pseudo-cubic cell edges formed by the Ti^{4+} ions. This leads to a non-180° Ti-O-Ti bond angle and the associated offset results in a long and short bond between the O^{2-} with Bi^{3+} along different directions. In contrast, the O3 position lies more closely to the edge and thus forms an ~180° Ti-O-Ti bond angle and results in nearly identical O-Bi bonds lengths along different directions. This differing oxygen configuration is consistent with the smaller splitting observed in the local Bi-O3 partial PDF when compared to that of Bi-O1 and Bi-O2.

An interesting implication of this anisotropic Bi-O bonding arrangement is the effect on the possible ferroelectric domain configurations and their polarization switching at the local level. From Figure 11c, it is rather obvious that the Bi^{3+} in the Bi-O3 plane would be stable under in-plane components of electric field compared to out-of-plane components and therefore, displacements in and out of this plane are more likely. This plane contrasts that shown in Figure 11a, where it is clear that electric field in the Bi-O1 plane can be associated with Bi^{3+} displacements and correlated displacements of the O1 atoms in and out of the Ti^{4+} pseudo-cubic box (i.e., oxygen inversion or switching between positions inside and outside of the Ti pseudo-cubic unit cell). Visual inspection also reveals that the same holds true for the Bi-O2 plane depicted in Figure 11b. Additional experimental and theoretical studies should be completed in

order to determine the extent to which this anisotropic bonding environment correlates with polarizability and polarization switching.

IV. Conclusions

Several recent studies have explored the differences between the short- and long-range structures of sodium bismuth titanate.[8, 20-22] The aim of this work was to build on these previous findings and better understand the nature of the differences between the local and average structure of NBT. For this purpose, the structure of NBT during two different states of the synthesis routine was investigated using X-ray and neutron scattering. Crystallographic refinement using the Rietveld method and combined X-ray and neutron diffraction data yielded a structure that represented the long-range, average structure. Pair distribution function (PDF) studies using total scattering X-ray and neutron data were used to determine local structure variations from this long-range average structure. A small box model approach was first used to model the local structure using the average structure of the material, as determined from Rietveld refinement. This approach revealed a larger departure from the average structure in the calcined than in the sintered material. This result in combination with the RMC model indicates that the extent, but not the type, of disorder may be different in calcined and sintered powders. The larger discrepancy in the calcined sample can also be attributed to a less accurate average model, due to the increased Bragg peak widths. In addition, the small box model was used to further rule out the presence of local A-site ordering in NBT, supporting earlier work.

Examination of the neutron PDF through a 'box-car fitting' method showed that bond environments change as a function of length scale in the material, and bond valence requirements for Bi^{3+} in particular are locally accommodated by disorder of the Bi-O bonds. The BVS of Bi^{3+}

in the average structure is significantly lower than the ideal value and could be a driving force for the departure of the local structure from the average. Since the small box model constrained Bi^{3+} and Na^{+} to the same position, changes in the O^{2-} positions affect both ions, and therefore the positions of the O^{2-} around Bi^{3+} sites on a local scale cannot be determined using this model. The RMC method more easily permits the positions of Na^{+} and Bi^{3+} to be unique, allowing the determination of their distinctive bonding environments with O^{2-}. This is clearly indicated by the asymmetry of the Bi-O partial pair distribution function, which is not present in the Na-O partial PDF (Fig. 8). Such a difference in the environments of Na^{+} and Bi^{3+} was also found in previous PDF studies of NBT from Jeong *et al*. and Keeble *et al*.[20, 21] This result supports the observations from the XAFS study by Shuvaeva *et al*., which stated that Bi^{3+} has a local environment that is more distorted than the average structure.[22] A closer examination of the average of the Na^{+} and Bi^{3+} distributions calculated in the RMC model revealed that the mean positions of the ions vary slightly from each other and from the average A-site position of the Rietveld model. Previous TEM studies of NBT from Levin and Reaney also reported disordered displacements of the A- and B-site cations.[8] The unique local bonding environment of Bi^{3+} with O^{2-} may be formed as a means for Bi^{3+} to achieve a BVS closer to its oxidation state as well as for the accommodation of the Bi^{3+} lone pair. The Bi^{3+} bonding environment determined in this work may be used to provide some insight into the formation of ferroelectric domains in this material.

Acknowledgements:

JJ and EA acknowledge partial support for this work from the U.S. National Science Foundation under award number DMR-0746902. JJ and JF acknowledge partial support for this work from the U.S. Department of the Army under W911NF-09-1-0435. JCN would like to acknowledge

the support by the U.S. National Science Foundation under award number DMR-0447910. This work has benefited from the use of the NPDF beamline at the Lujan Center at the Los Alamos Neutron Science Center, funded by the US DOE Office of Basic Energy Sciences. Los Alamos National Laboratory is operated by Los Alamos National Security LLC under DOE contract No. DE-AC52- 06NA25396. The upgrade of NPDF has been funded by NSF through Grant No. DMR 00-76488. Use of the 11-BM and 11-ID-B beamlines at the Advanced Photon Source, an Office of Science User Facility operated for the U.S. Department of Energy (DOE) Office of Science by Argonne National Laboratory, was supported by the U.S. DOE under Contract No. DE-AC02-06CH11357. Helpful discussion on this work with Prof. Pam Thomas and Dr. Dean Keeble are gratefully acknowledged.

References

[1] J. R□del, W. Jo, K. Seifert, E. Anton, T. Granzow, and D. Damjanovic, Journal of the American Ceramic Society **92**, 1153 (2009).

[2] G. A. Smolenskii, V. A. Isupov, A. I. Agranovskaya, and N. N. Krainik, *Soviet Physics-Solid State*, 1961), Vol. 2, p. 2651.

[3] G. O. Jones and P. A. Thomas, Acta Crystallographica Section B-Structural Science **58**, 168 (2002).

[4] S. Gorfman and P. A. Thomas, Journal of Applied Crystallography **43**, 1409 (2010).

[5] E. Aksel, J. Forrester, J. Jones, P. Thomas, K. Page, and M. Suchomel, Applied Physics Letters **98** (2011).

[6] V. Dorcet and G. Trolliard, Acta Mater. **56**, 1753 (2008).

[7] R. Beanland and P. A. Thomas, Scripta Materialia **65**, 440 (2011).

[8] I. Levin and I. M. Reaney, Advanced Functional Materials **22**, 3445 (2012).

[9] M. Groting, S. Hayn, and K. Albe, Journal of Solid State Chemistry **184**, 2041 (2011).

[10] S. J. L. Billinge and I. Levin, Science **316**, 561 (2007).

[11] T. Egami and S. J. L. Billinge, *Underneath the Bragg peaks : structural analysis of complex materials* (Pergamon, Kiddington, Oxford, UK ; Boston, 2003).

[12] C. A. Young and A. L. Goodwin, Journal of Materials Chemistry **21**, 6464 (2011).

[13] T. Proffen and K. L. Page, Zeitschrift für Kristallographie **219**, 130 (2004).

[14] V. Krayzman and I. Levin, Journal of Applied Crystallography **41**, 386 (2008).

[15] T. Egami, S. Teslic, W. Dmowski, D. Viehland, and S. Vakhrushev, Ferroelectrics **199**, 103 (1997).

[16] T. Egami, W. Dmowski, M. Akbas, and P. K. Davies, AIP Conference Proceedings **436**, 1 (1998).

[17] V. Petkov, M. Gateshki, M. Niederberger, and Y. Ren, Chemistry of Materials **18**, 814 (2006).

[18] A. L. Goodwin, S. A. T. Redfern, M. T. Dove, D. A. Keen, and M. G. Tucker, Physical Review B **76**, 174114 (2007).

[19] K. Page, T. Kolodiazhnyi, T. Proffen, A. K. Cheetham, and R. Seshadri, Physical Review Letters **101**, 205502 (2008).

[20] I. Jeong, C. Park, D. Kim, S. Kim, B. Moon, W. Kim, and C. Ahn, Zeitschrift Fur Kristallographie **226**, 150 (2011).

[21] D. S. Keeble, E. R. Barney, D. A. Keen, M. G. Tucker, J. Kreisel, and P. A. Thomas, Advanced Functional Materials **23**, 185 (2013).

[22] V. A. Shuvaeva, D. Zekria, A. M. Glazer, Q. Jiang, S. M. Weber, P. Bhattacharya, and P. A. Thomas, Physical Review B **71**, 174114 (2005).

[23] P. A. Doyle and P. S. Turner, *Acta Cryst. A* **24**, 390 (1968).

[24] V. F. Sears, Neutron News **3**, 26 (1992).

[25] M. Davies, E. Aksel, and J. Jones, Journal of the American Ceramic Society **94**, 1314 (2011).

[26] T. Proffen, T. Egami, S. J. L. Billinge, A. K. Cheetham, D. Louca, and J. B. Parise, Appl. Phys. A **74 [Suppl.]**, S163 (2002).

[27] P. F. Peterson, Gutmann, M., Proffen, Th., Billinge, S. J. L., Journal of Applied Crystallography **33**, 1192 (2000).

[28] A. P. Hammersley, Svensson, S. O., Hanfland, M., Fitch, A. N., Hausermann, D., High Pressure Research **14**, 235 (1996).
[29] X. Qiu, Thompson, J. W., Billinge, S. J. L., J. Appl. Cryst. **37**, 678 (2004).
[30] A. C. Larson and R. B. Von Dreele, General Structure Analysis System (GSAS), Los Alamos National Laboratory Report LAUR, 86 (2000).
[31] B. H. Toby, J. Appl. Cryst. **34**, 210 (2001).
[32] C. L. Farrow, Juhas, P, Liu, J W, Bryndin, D, Božin, E S, Bloch, J, Proffen, Th, Billinge, S J L, Journal of Physics: Condensed Matter **19**, 335219 (2007).
[33] B. H. Toby, Egami, T., Acta. Cryst. A **48**, 336 (1992).
[34] M. G. Tucker, D. A. Keen, M. T. Dove, A. L. Goodwin, and Q. Hui, Journal of Physics: Condensed Matter **19**, 335218 (2007).
[35] D. Keen, Journal of Applied Crystallography **34**, 172 (2001).
[36] N. E. Brese, O'Keeffe, M., Acta. Cryst. B **47**, 192 (1991).
[37] X. Qiu, T. Proffen, J. F. Mitchell, and S. J. L. Billinge, Physical Review Letters **94**, 177203 (2005).
[38] X. Qiu, J. W. Thompson, and S. J. L. Billinge, Journal of Applied Crystallography **37**, 678 (2004).
[39] D. P. Shoemaker, R. Seshadri, A. L. Hector, A. Llobet, T. Proffen, and C. J. Fennie, Physical Review B **81**, 144113 (2010).

Figure Captions

FIG. 1. (Color Online) Powder diffraction patterns of sintered (x) and calcined (x) NBT powders from neutron and X-ray diffraction. The results of a calculated fit (-) using both the X-ray and neutron diffraction patterns for each type of powder is also shown. Reflection markers for the *Cc* phase are shown as vertical lines with the difference pattern below the diffraction pattern. The labeled peak indices are relative to the pseudocubic perovskite unit cell. The refined Bragg R values (R_w) of each fit are also indicated in the figure.

FIG. 2. (Color Online) The NBT unit cell is shown on the left, where the green and black circles represent the A site, the O sites are shown as orange circles, and the Ti site is in the center of the blue octahedron. The four figures in the middle are Fourier maps represented as 3D isosurfaces showing the total scattering density in the NBT unit cell for neutron and X-ray Bragg profiles. Only the A site and Ti site are shown for X-ray maps, while the neutron maps include O sites. The light blue surfaces in the neutron maps indicate the negative scattering density of Ti. X-ray scattering densities on the A-sites are shown on the far right along the monoclinic (001) plane, with only spherical intensity present.

FIG. 3. (Color Online) Results of fitting 1-20 Å X-ray $G(r)$s (a,b) and neutron $G(r)$s (c,d) with the *Cc* average structure model for sintered and calcined NBT samples. Data are shown as black circles, fits are given as purple and orange lines (for calcined and sintered samples, respectively) and difference curves have been offset below the data and fits in black. Refined goodness of fit parameters (R_w) are given in each panel. Note X-ray and neutron data are shown on different intensity scales.

FIG. 4. (Color Online) Exploring *A*-site ordering: (a) 10 Å PDF Refinement R_w values (goodness of fit) for sintered (black) and calcined (purple) data sets with different fractions of mixed-site *A* cation and layered *A* cation structure models. Neutron results are given with circles and solid lines through the points, while x-ray results are given with squares and dashed lines through the points. In the bottom two panels, 10 Å X-ray (b) and neutron (c) PDF calculations are displayed for the two end-member model structures (at fraction of layered phase = 0 and 1). The random structure calculations are shown in black dash lines and the layered structure calculations are displayed in blue solid lines.

FIG. 5. (Color Online) Calculated (Bi/Na)-O (a) and (b) as well as Ti-O (c) and (d) bond lengths from the 'box-car fitting' method are shown for both calcined and sintered NBT. The box plots at each *r* value indicate the spread in the bond lengths for that calculation. The edges of the box represent one standard deviation from the mean and the whiskers are the minimum and maximum values. The closed symbols for each data set are the mean values while the open symbols show all of the bond lengths. The solid line in each plot is the average bond length calculated from the atomic positions refined through the Rietveld method and the dashed lines show one standard deviation from the mean. The inset in each plot shows the average bond lengths from the 'box-car fitting' on a smaller y-scale for clarity (all insets have the same y-range).

FIG. 6. The calculated BVS for Bi^{3+} (a), Na^{+} (b) and Ti^{4+} (c) is shown for the calcined and sintered materials. The dashed and solid lines in the plots represent the BVS calculated from the average structure obtained by the Rietveld method for calcined and sintered NBT, respectively. The y-axis scales are identical in all three panels.

FIG. 7. (Color Online) Reverse Monte Carlo fits to the neutron PDF of (a) calcined and (b) sintered NBT. Data are shown as black dots, fits as colored lines, and a difference curve falls below. Both simulations are conducted with BVS constraints to maintain the nominal cation valences.

FIG. 8. (Color Online) Folded RMC models produce "point clouds" of atoms at each crystallographic site. No significant differences are seen when a single model is plotted to show only Na^{+} (a) and Bi^{3+} (b) cations, implying that Bi^{3+} does not simply displace off-center, and does not have significantly larger displacement than Na^{+}.

FIG. 9. (Color Online) Partial pair distribution functions from the RMC model of a sintered sample give nearly symmetric bond distance distributions of Na-O (a). Tick marks between the two panes show the Rietveld-refined bond distances in the *Cc* cell. For Bi-O in (b), the asymmetry seen in the *Cc* cell is greatly amplified. Distances are shown to each of the three distinct O atoms on 4*a* sites in the *Cc* cell. Results for calcined samples were similar.

FIG. 10. (Color Online) The distribution of the Na^{+} and Bi^{3+} ions relative to the average A-site position. The x and y directions are along the *a* and *b* unit cell axes, and z is orthogonal to them.

FIG. 11. (Color Online) Pseudo-cubic representation of the NBT unit cell showcasing the arrangement of the three unique oxygen lattice positions relative to the Bi-site. A) O1, B) O2, and C) O3 positions.

Table I - Refined atomic positions in fractional coordinates for calcined and sintered NBT from a combined X-ray and neutron refinement via the Rietveld method, and 1.5 to 20 Å range PDF fit results for the X-ray and neutron data.

Calcined NBT					Sintered NBT				
Site		Rietveld	Neutron PDF	X-ray PDF	Site		Rietveld	Neutron PDF	X-ray PDF
Ti	x	0.2628(4)	0.247(2)	0.23140(7)	Ti	x	0.2592(4)	0.258(2)	0.28510(2)
	y	0.2580(6)	0.248(2)	0.2516(9)		y	0.2553(7)	0.256(3)	0.2493(8)
	z	0.7451(8)	0.712(1)	0.69382(4)		z	0.7335(6)	0.709(3)	0.75481(9)
O1	x	0.0085(6)	-0.013(2)		O1	x	-0.0024(4)	-0.008(2)	
	y	0.2093(3)	0.1925(9)	Not		y	0.1997(2)	0.188(1)	Not
	z	0.467(1)	0.433(2)	refined,		z	0.4585(8)	0.452(4)	refined,
O2	x	0.2090(3)	0.213(2)	values	O2	x	0.1991(2)	0.217(3)	values
	y	0.4931(6)	0.518(1)	set to		y	0.4853(5)	0.519(2)	set to
	z	-0.0777(7)	-0.099(2)	neutron		z	-0.076(1)	-0.089(3)	neutron
O3	x	0.2648(4)	0.265(2)	PDF	O3	x	0.2577(2)	0.263(3)	PDF
	y	0.0137(6)	0.003(2)	results		y	0.0110(5)	0.009(3)	results
	z	0.0104(8)	-0.035(2)			z	-0.010(1)	-0.022(4)	

Table II - Refined isotropic atomic displacement parameters in unites of $Å^2$ for calcined and sintered NBT from a combined X-ray and neutron refinement via the Rietveld method, and 1.5 to 20 Å range PDF fit results for the X-ray and neutron data.

Calcined NBT				Sintered NBT			
Element	Rietveld ($Å^2$)	Neutron PDF ($Å^2$)	X-ray PDF ($Å^2$)	Element	Rietveld ($Å^2$)	Neutron PDF ($Å^2$)	X-ray PDF ($Å^2$)
Na/Bi	3.90(1)	2.2(1)	1.941(2)	Na/Bi	3.86(1)	1.93(5)	1.1767(6)
Ti	0.31(2)	0.67(7)	0.615(2)	Ti	0.05(2)	0.75(4)	1.799(3)
O1	1.08(2)	0.97(7)		O1	0.39(3)	0.82(4)	
O2	1.71(2)	1.45(9)	6.85(1)	O2	1.33(5)	0.84(5)	3.774(5)
O3	2.04(2)	2.06(9)		O3	1.88(4)	1.88(7)	

Figure 1

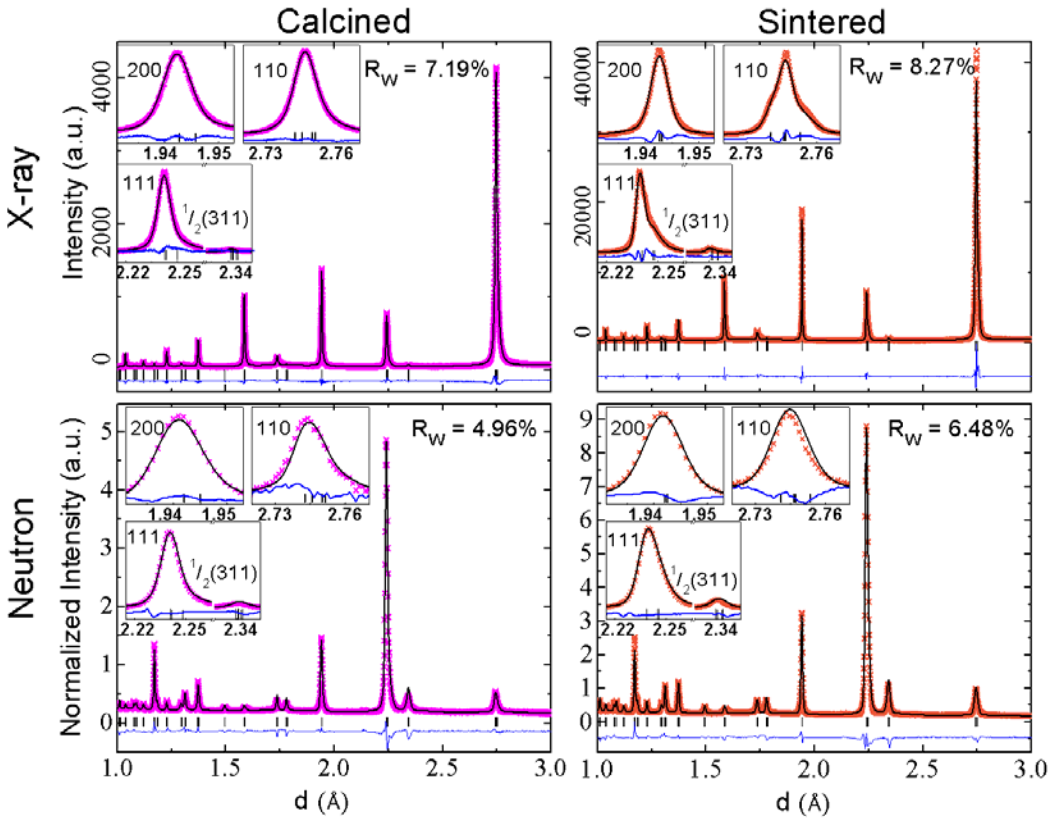
Calcined
Sintered
X-ray
Neutron
Intensity (a.u.)
Normalized Intensity (a.u.)
R_W = 7.19%
R_W = 8.27%
R_W = 4.96%
R_W = 6.48%
200
110
111
$^1/_2$(311)
1.94 1.95
2.73 2.76
2.22 2.25 2.34
d (Å)

Figure 2

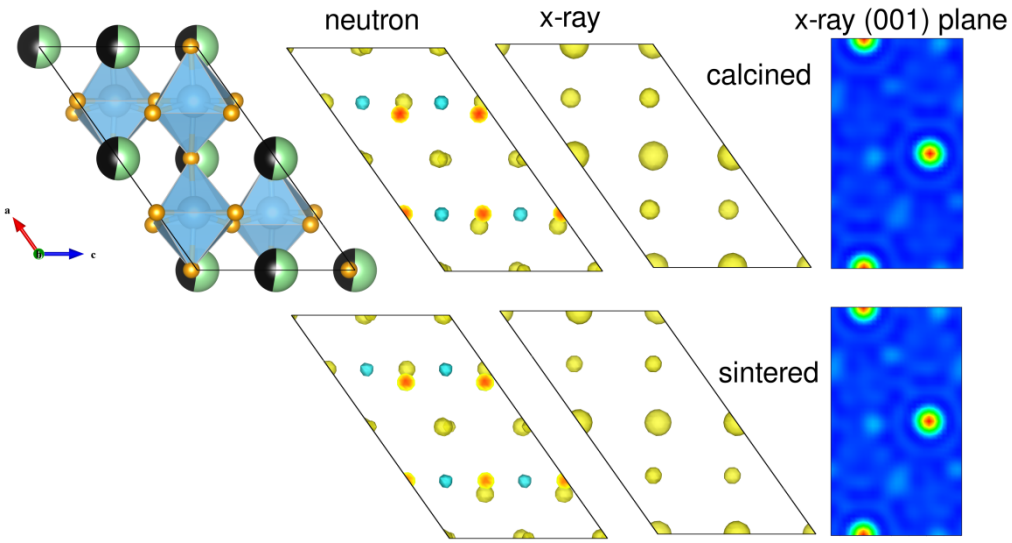

Figure 3

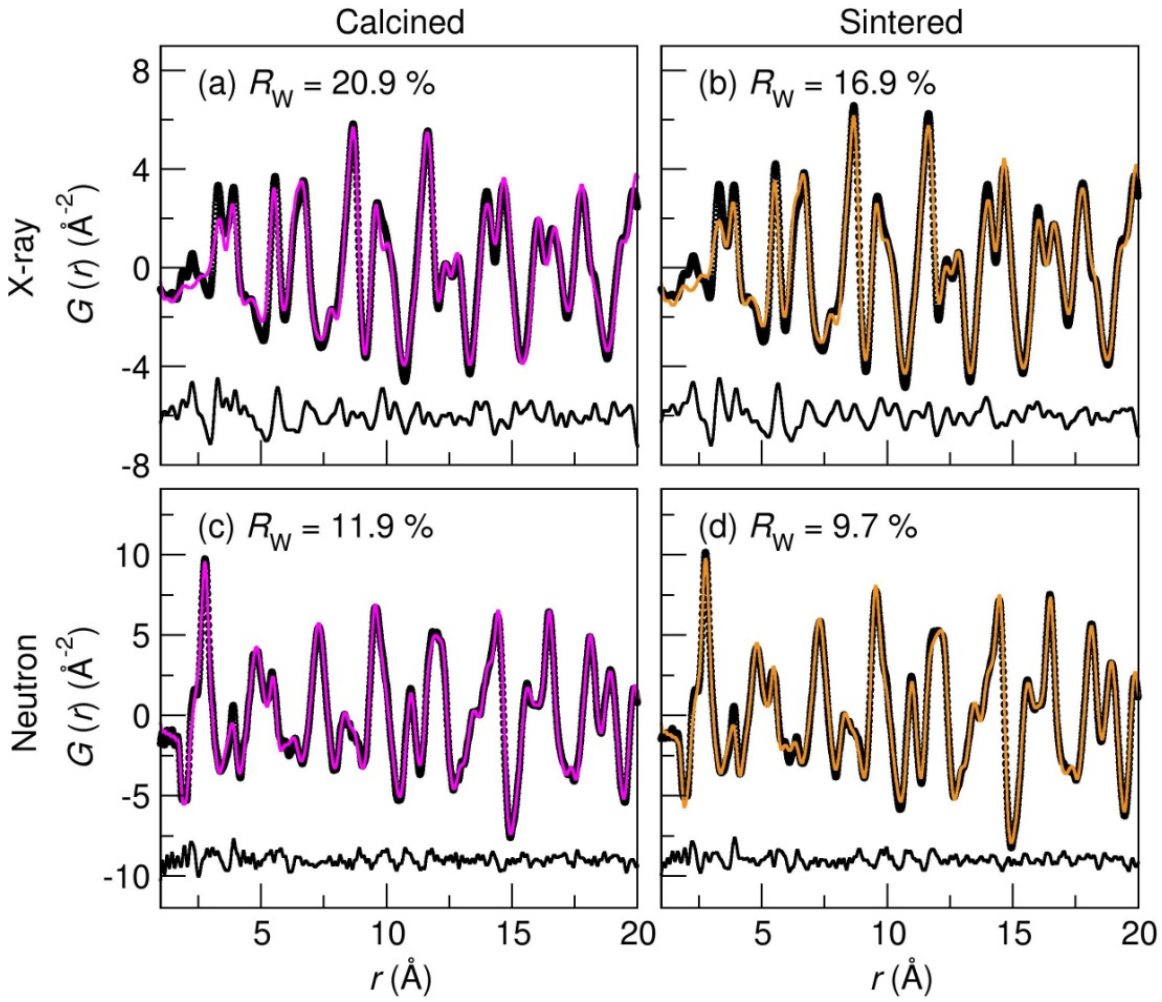
Calcined
Sintered
(a) R_W = 20.9 %
(b) R_W = 16.9 %
(c) R_W = 11.9 %
(d) R_W = 9.7 %
X-ray
Neutron
$G(r)$ (Å^{-2})
r (Å)

Figure 4

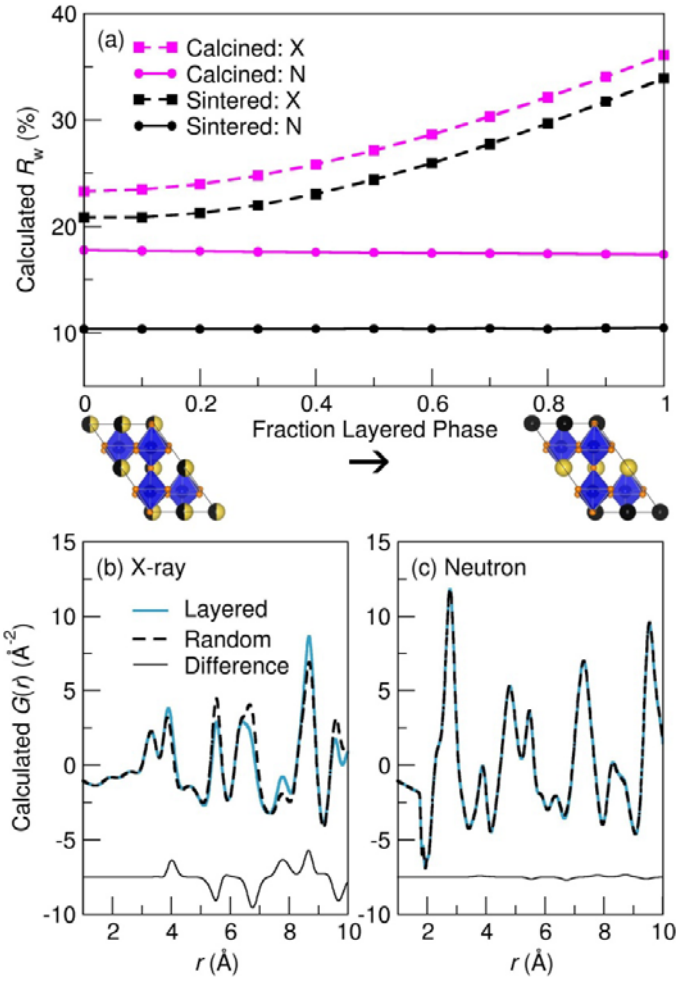
(a)
Calcined: X
Calcined: N
Sintered: X
Sintered: N
Calculated R_w (%)
Fraction Layered Phase
(b) X-ray
Layered
Random
Difference
Calculated $G(r)$ (Å^{-2})
r (Å)
(c) Neutron
r (Å)

Figure 5

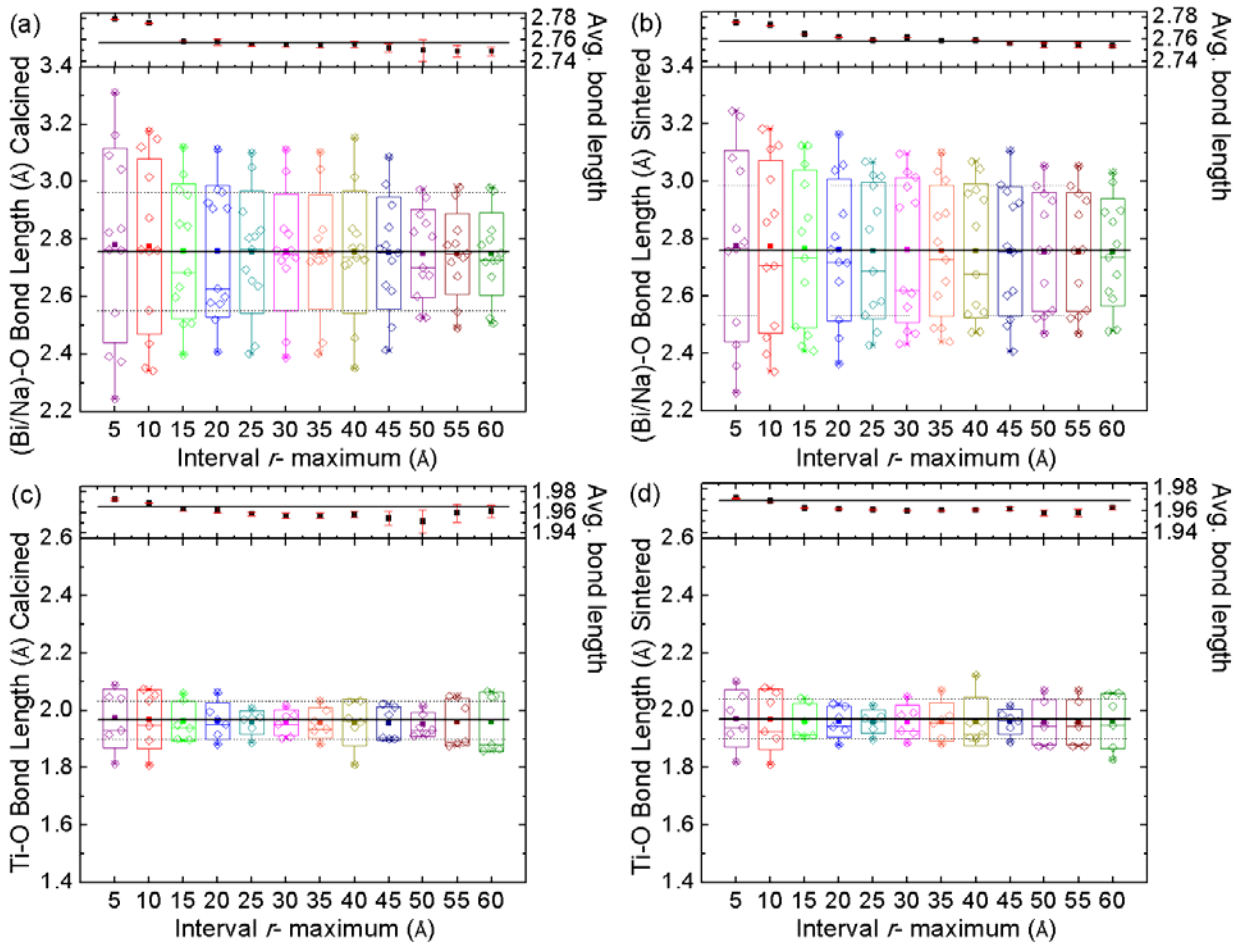
(a)
(Bi/Na)-O Bond Length (Å) Calcined
Avg. bond length
Interval r- maximum (Å)
(b)
(Bi/Na)-O Bond Length (Å) Sintered
Avg. bond length
Interval r- maximum (Å)
(c)
Ti-O Bond Length (Å) Calcined
Avg. bond length
Interval r- maximum (Å)
(d)
Ti-O Bond Length (Å) Sintered
Avg. bond length
Interval r- maximum (Å)

Figure 6

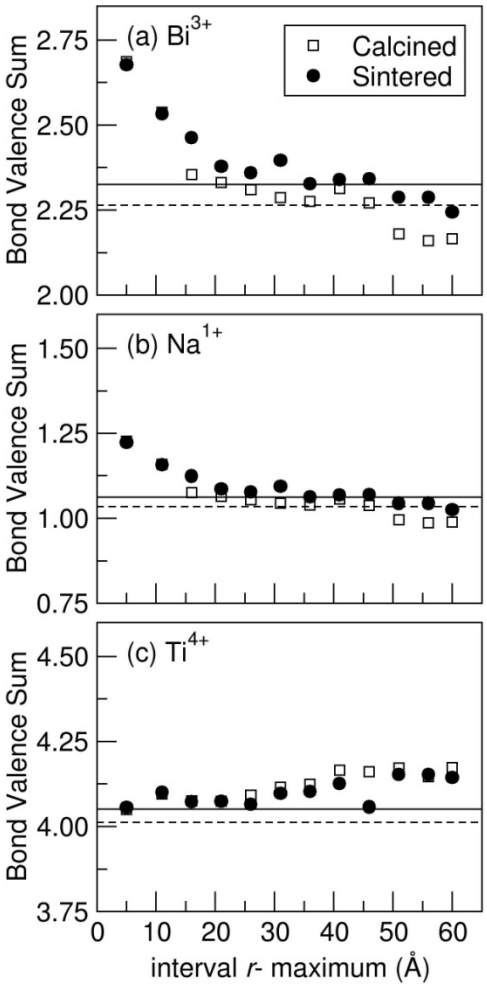
(a) Bi3+
Calcined
Sintered
Bond Valence Sum
2.75
2.50
2.25
2.00
(b) Na1+
Bond Valence Sum
1.50
1.25
1.00
0.75
(c) Ti4+
Bond Valence Sum
4.50
4.25
4.00
3.75
0
10
20
30
40
50
60
interval r- maximum (Å)

Figure 7

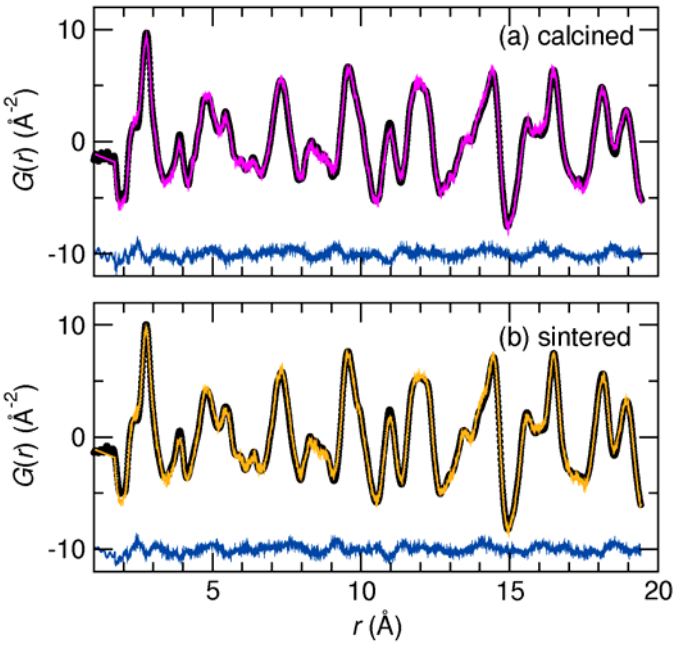

Figure 8

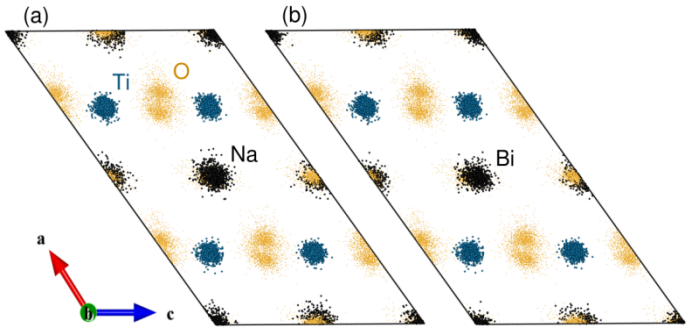

Figure 9

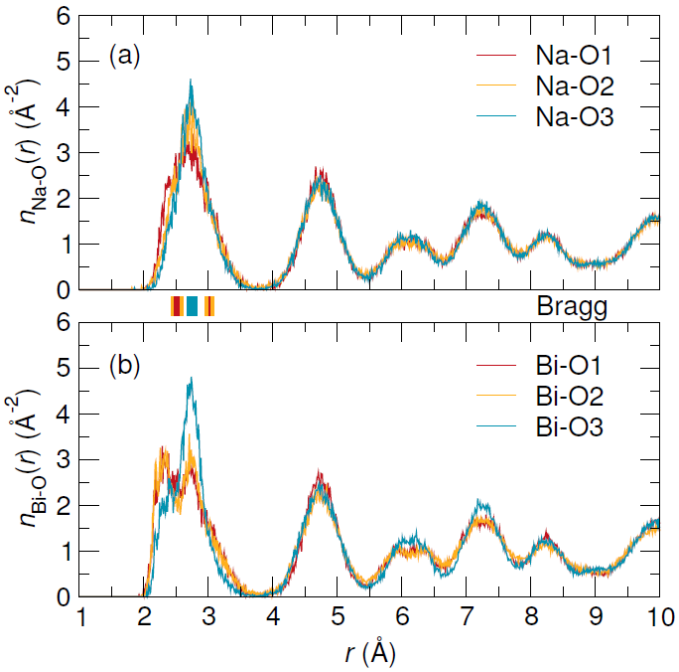

Figure 10

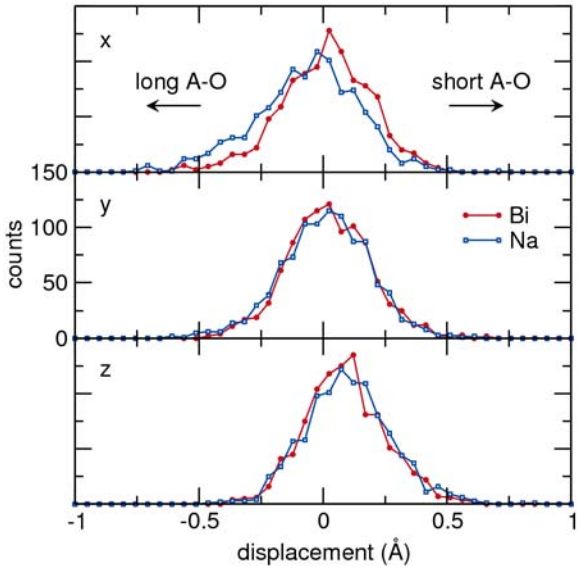
x
long A-O
short A-O
150
y
Bi
Na
counts
100
50
0
z
-1
-0.5
0
0.5
1
displacement (Å)

Figure 11